

Quantum chaos associated with emergent event horizon in transition layer between type-I and type-II Weyl semimetals

Yu-Ge Chen^{1,2,3,*}, Xi Luo^{4,*}, Fei-Ye Li^{1,2,3}, Bin Chen⁴, and Yue Yu^{1,2,3}

1. State Key Laboratory of Surface Physics, Fudan University, Shanghai 200433, China

2. Center for Field Theory and Particle Physics, Department of Physics, Fudan University, Shanghai 200433, China

3. Collaborative Innovation Center of Advanced Microstructures, Nanjing 210093, China

4. College of Science, University of Shanghai for Science and Technology, Shanghai 200093, PR China

(Dated: December 15, 2024)

We present pairwise emergent event horizons in a transition layer between type-I and type-II Weyl semimetals (WSMs). The Hawking temperature defined by a novel surface gravity at the horizon is in a measurable interval. On the type-II WSM side, i.e., inside the horizons, the motion of the quasiparticles may be chaotic inside a critical surface as they are governed by an effective inverted oscillator potential induced by the mismatch between the type-I and type-II Weyl nodes. In a relevant lattice model, we calculate out of time ordered correlators (OTOCs). We find that the OTOCs are fast scrambling with a quantum Lyapunov exponent in high temperature and the scrambling is saturated after the Ehrenfest time. This confirms the quantum chaotic behavior.

Introductions. Recent developments on the frontier of theoretical physics research have entangled the black hole horizon physics with quantum chaos [1–7].

In condensed matter systems, the black hole analog had been pioneered by Unruh in transsonic fluid flow [8]. A quantum analog had been provided in Bose-Einstein condensation [9, 10], and a magnonic black hole was predicted [11]. The exotic emergent geometries (or gravities) have also been studied in Fermi surface [12], fractional quantum Hall effects [13–16], graphene [17], deformed crystal [18], type-II Weyl semimetal (WSM) [19–22], and type-III Dirac semimetal [23]. Several systems may simulate the Hawking evaporation at a black hole event horizon [24, 25]. However, the chaotic behaviors at the horizon do not appear easily. For instance, for the trajectory of a moving particle outside of the horizon to be chaotic classically, there must be an external potential near the horizon [26]. The Lyapunov exponent is subject to a maximal chaotic bound, the surface gravity [1]. This bound is saturated for theories with AdS/CFT duality, such as the case in the Sachdev-Ye-Kitaev model [2–4].

Volovik et al recently studied the emergent metric in the inhomogeneous WSM [19–21]. They found a general correspondence between the emergent vielbein e_μ^i and the effective Hamiltonian near a Weyl node $\mathbf{K} = (K_x, K_y, K_z)$, i.e., $H(\vec{q}) = e_\mu^i q_i \sigma^\mu$, where $\mu = 0, i$ with $i = x, y, z$. $q_i = k_i - K_i$ and $\sigma^\mu = (I, \sigma^i)$ are the identity and Pauli matrices. Here the Einstein's summation convention for repeated indices is used. The 'speed of light' v_F (the Fermi velocity), the electron band mass m_b , and \hbar are set to be unity unless they are explicitly restored. The spectrum is given by $E(Q_i)_\pm = e_0^j [e^{-1}]_j^i Q_i \pm |\mathbf{Q}|$ with $Q_i \equiv e_i^j q_j$. The vielbein components e_μ^i together with $e_0^0 = -1$ and $e_i^0 = 0$ define an emergent metric $g^{\mu\nu} = \eta^{\alpha\beta} e_\alpha^\mu e_\beta^\nu$ with the signature $\eta^{\mu\nu} = \text{diag}(-1, 1, 1, 1)$

[19]. The event horizon of this emergent geometry is determined by $|\mathbf{v}| = 1$ where $v^i = e_0^j [e^{-1}]_j^i$. A Weyl node is called type-I (type-II) if $|\mathbf{v}| < 1$ ($|\mathbf{v}| > 1$). Notice that the type of each one in a pairwise nodes can be arbitrary [27, 28].

Volovik uses the spherically symmetric metric to study inhomogeneous WSM [20] but it is difficult to be realized in reality. Both type-I and type-II WSMs have been found [29–35]. In order to simulate an event horizon in a realizable geometry and study the chaos phenomena, we consider a type-I/type-II WSM transition layer (TL) where the type-I and type-II Weyl nodes may mismatch (See Fig. 1(a)). Within the TL, a black/white hole planar horizon emerges effectively at a plane with $|\mathbf{v}| = 1$ in the TL. That is, the interpolation between the type-I and type-II WSM Hamiltonians. induces a columnar surface gravity. A fermionic shock wave and the Hawking evaporation are possible to be detected because the Hawking temperature may be as high as several tens of Kelvin.

In the effective Hamiltonian approach, we further find that when the Weyl nodes of the type-I and type-II do not completely match, the TL states inside and outside the horizon may be totally different: On the type-I WSM side, the TL state is described by the Landau levels of the WSM in an effective magnetic field. On the type-II side, after a characteristic plane, the TL states are governed by an effective inverted oscillator potential [36–38] and thus are chaotic due to the non-integrability caused by coupling to the environment potential [26].

In order to verify the sensitivity to the initial condition of the quasiparticles in the TL, we study a lattice model which reduces to the effective chaotic model in the TL in the long wave length limit. We calculate out of time ordered correlators (OTOCs) of the quantum states which characterize the quantum chaotic behavior [1–7, 39]. For a proper hopping strength in the TL with a sufficient layer thickness, we find that in a lower temperature, the OTOC does not show a fast scrambling over a short time while it does when the temperature is higher and a quantum Lyapunov exponent is obtained. The OTOCs sat-

*These two authors contribute equally.

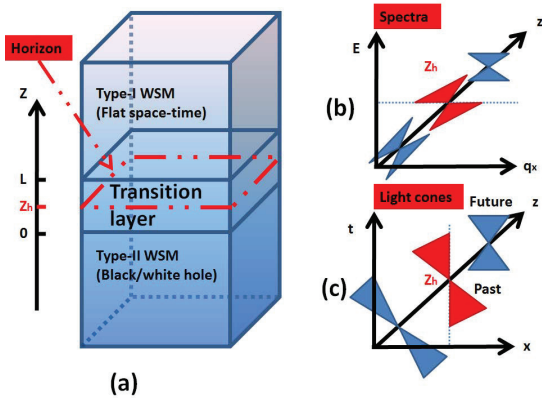


FIG. 1: (color online) (a) The TL between Type-I and Type-II WSMs. The critical surface $z = z_h$ serves as the horizon. (b) The spectra outside of, at and inside of the horizon, corresponding to type-I, critical and type-II WSM's. (c) The light cones outside of, at and inside of the horizon. In (b) and (c), we take $\alpha_z(z) = 0$ and project to the x -direction for simplicity.

urate after the Ehrenfest time. These two properties of OTOC indicate the existence of quantum chaos inside the horizon [40].

Effective model for TL. We consider that type-I and type-II WSMs couple as shown in Fig.1(a). The TL is located between $z = 0$ and $z = L$. Assuming \mathbf{K}^I (\mathbf{K}^{II}) is a Weyl node of the type-I (type-II) WSM in the regime $z > L$ ($z < 0$), and $|\mathbf{K}^I - \mathbf{K}^{II}| \ll K_0$ where K_0 is the distance between a pair of Weyl nodes in the bulk. The effective Hamiltonian in the bulk of the type-I/II WSM is given by

$$H_{I/II} = (k_i - K_i^{I/II})\sigma^i - \alpha_{x,I/II}(k_x - K_x^{I/II}) - \alpha_{z,I/II}(k_z - K_z^{I/II}), \quad (1)$$

where $\alpha_{I/II} = (\alpha_{x,I/II}, 0, \alpha_{z,I/II})$ are parameters that tilt the Dirac cones. For the type-I WSM, $|\alpha_I| = \sqrt{\alpha_{xI}^2 + \alpha_{zI}^2} < 1$ and $|\alpha_{II}| = \sqrt{\alpha_{xII}^2 + \alpha_{zII}^2} > 1$ for the type-II WSM. We further assume $|\Delta\alpha| = |\alpha_{II} - \alpha_I| \ll 1$. The TL effective Hamiltonian can be approximated by a linear interpolation between H_I and H_{II} [41]

$$H(z) = H_{II} + (H_I - H_{II})\frac{z}{L}, \quad (2)$$

where $0 \leq z \leq L$. Defining $\mathbf{q} = \mathbf{k} - \mathbf{K}^{II}$ and $B_i = \frac{K_i^I - K_i^{II}}{L} = \frac{\Delta K_i}{L}$,

$$H(z) = (q_x + B_x z)\sigma^x + (q_y + B_y z)\sigma^y + (-i\partial_z + B_z z)\sigma^z - \alpha_x(z)(q_x + B_x z) - \alpha_z(z)(-i\partial_z + B_z z) + \dots \quad (3)$$

where “...” are high order terms including $O(\Delta\mathbf{K} \cdot \Delta\alpha)$ etc. q_z is replaced by $-i\partial_z$ and B_x (B_y) can be thought as an effective magnetic field in the y (x)-direction. If an environment potential $V(x, y)$ in the x - y plane is introduced, (q_x, q_y) are replaced by $(-i\partial_x, -i\partial_y)$. For simplicity, we will add the environment later. One can perform a

gauge transformation to change $-i\partial_z + B_z z$ to $-i\partial_z$ if the wave function ψ changes to $e^{-i\frac{B_z z^2}{2}}\psi$ accordingly. $\alpha(z)$ is a linear interpolation like $H(z)$, i.e., $\alpha(z) = \alpha_{II} - \Delta\alpha\frac{z}{L}$. Since $|\Delta\alpha| \ll 1$, $\alpha(z)$ is a slow varying vector function of z . $|\alpha(z_h)| = 1$ determines the critical surface with $z = z_h$ which separates the type-I and type-II WSM, where

$$\frac{z_h}{L} = \frac{\Delta\alpha \cdot \alpha_{II} - \sqrt{(\Delta\alpha \cdot \alpha_{II})^2 - (\Delta\alpha)^2(\alpha_{II}^2 - 1)}}{(\Delta\alpha)^2} \quad (4)$$

Emergent geometry and horizon. To see the emergent geometry, we first consider $B_i = \frac{\Delta K_i}{L} = 0$ for simplicity. The TL Hamiltonian (3) reduces to Volovik's expression with $e_0^x = -\alpha_x(z)$, $e_0^z = -\alpha_z(z)$, $e_0^y = 0$ and $e_j^i = \delta_j^i$. Thus, $v^i = -\alpha_i(z)$ and $|\mathbf{v}| = |\alpha(z)| = \sqrt{\alpha_x^2 + \alpha_z^2}$. The effective geometry in the TL is described by the line element of the induced metric [19] $ds^2 = g^{\mu\nu}dx_\mu dx_\nu = -(1 - |\mathbf{v}(z)|^2)dt^2 - 2\mathbf{v}(z) \cdot d\mathbf{r}dt + (d\mathbf{r})^2$. Defining a proper time by $d\tau = dt + \frac{\mathbf{v}(z) \cdot d\mathbf{r}}{1 - |\mathbf{v}|^2}$ so that the space and time do not mix in the line element that in the cylinder coordinate with a radius $\rho = \sqrt{x^2 + z^2}$ is given by $ds^2 = -(1 - |\mathbf{v}|^2)d\tau^2 + \frac{d\rho^2}{1 - |\mathbf{v}|^2} + \rho^2 d\varphi^2 + dy^2$. The property of the geometry defined by this metric is dependent on the sign of $\alpha_\rho = \alpha \cdot \rho / \rho$. For $\alpha_\rho > 0$ ($\alpha_\rho < 0$), the geometry is black (white) hole-like [19]. The event horizon is determined by $|\mathbf{v}(z)| = |\alpha(z)| = 1$ which is exactly at the critical surface with $z = z_h$. For illustration, we show the spectra and light cones with $\alpha_z(z) = 0$ in Fig. 1 (b) and (c).

Normally, for an isotropic metric, the surface gravity at the event horizon is defined by the normal derivative of the velocity component normal to the horizon. Here it is $\eta_z = \frac{\partial v_z(z)}{\partial z}|_{z=z_h} = -\frac{\Delta\alpha_z}{L}$. For WSMs, it is often the case that $\Delta\alpha_z = 0$ and then $\eta_z = 0$. Because the non-zero value of the tangent vector $v_x(z)$ breaks the isotropy at the horizon, we can define a columnar surface gravity, which may characterize more interesting behaviors of the TL. This is defined by $\eta_\rho = \frac{\partial |\mathbf{v}(z)|}{\partial z}|_{z=z_h} = \Delta\alpha \cdot \alpha(z_h)\frac{v_F}{L}$. The Hawking temperature of this emergent black hole horizon is defined by

$$T_H = \frac{\hbar\eta_\rho}{2\pi k_B} = \frac{\Delta\alpha \cdot \alpha(z_h)\hbar v_F}{2L\pi k_B}. \quad (5)$$

The typical value of the Fermi velocity for WSM is $v_F \sim 10^6$ m/s. If the thickness of the TL $L \lesssim 10$ nm, $T_H \gtrsim 10^2 \Delta\alpha \cdot \alpha(z_h)$ K. If $\Delta\alpha \cdot \alpha(z_h) \sim 0.1$, the Hawking temperature may arrive at several tens of Kelvin which are experimentally reachable. In principle, a Hawking evaporation may be observed by a thermal spectrum of the TL fermion when the layer are forming [20, 42]. Similar to the transsonic wave in the bosonic fluid [8, 43], we have a fermion shock wave with a velocity $\mathbf{v}(z)$.

Chaotic transition layer. To show the chaos, we return to $0 < \Delta K_i \ll K_0$. From the effective model perspective, we try to solve the Dirac equation

$$H(z)\psi(z, t) = i\dot{\psi}(t), \quad (6)$$

where $H(z)$ is given by Eq. (3) and $\psi^T = (\chi, \zeta)$ is a two-component spinor. χ and ζ are coupled in Eq. (6) and we solve $\zeta = \zeta[\chi(z)]$. Without loss of generality, we take $q_y = 0$. Because $\alpha(z)$ slowly varies, we neglect $\partial_z \alpha(z)$ term in $\zeta[\chi(z)]$. Then, the dominant part of χ 's equation in the large \tilde{z} limit reads

$$\ddot{\chi} - \partial_{\tilde{z}}^2 \chi + [\kappa \tilde{z}^2 + B_y^2 (q_x^2 - \frac{2\sqrt{1-\alpha_z^2}}{B_x} q_x \tilde{z})] \chi + \dots = 0, \quad (7)$$

where $\tilde{z} = \frac{q_x + B_x z}{B_x \sqrt{1-\alpha_z^2}}$ and $\kappa = (1 - \alpha^2) B_x^2 + (1 - \alpha_z^2) B_y^2$ (See Appendix A for “...” terms in more details). For $\kappa = \omega^2 > 0$ and a fixed q_x , Eq. (7) coincides with the Landau levels of a Weyl fermion. When $z > z_h$, outside of the horizon, it happens.

When $|\alpha| > 1$ and $|\alpha_z| < 1$ [44], i.e., inside the horizon, it is possible that $\kappa < 0$ after $z < z_c$, a characterized plane with $z_c \leq z_h$ ($z_c = z_h$ if $B_y = 0$). We now introduce an environment potential $V(x)$ and then Eq. (7) becomes

$$\begin{aligned} \ddot{\chi} - \partial_{\tilde{z}}^2 \chi - \lambda_L^2 \tilde{z}^2 \chi - B_y^2 \partial_x^2 \chi + \epsilon_3 \tilde{z}^3 \chi + \epsilon_4 \tilde{z}^4 \chi \\ + 2i B_y^2 B_x^{-1} \sqrt{1 - \alpha_z^2} \tilde{z} \partial_x \chi + V(x) \chi = 0, \end{aligned} \quad (8)$$

where $\lambda_L^2 = (\alpha_{II}^2 - 1) B_x^2 + (\alpha_{z,II}^2 - 1) B_y^2 > 0$, $\epsilon_3 \sim O(\Delta \alpha \cdot \alpha_{II})$, and $\epsilon_4 \sim O((\Delta \alpha)^2) > 0$ (See Appendix A). If $V(x) = 0$, Eq. (8) is integrable and basically describes an inverted oscillator [36–38]. It is known that an inverted oscillator leads to the chaotic dynamics when it couples to the environment $V(x)$ [26, 45, 46]. Thus, the TL state when $z < z_c$ is chaotic and λ_L plays a role of the Lyapunov exponent. To illustrate, we have studied a steady state solution of (8) and thought $E^2 = \mathcal{E}$ as a classical energy. The Poincaré sections for the classical limit of (8) with $V(x) \sim x^2$ show that the Kolmogorov-Arnold-Moser tori keep nice periodic orbits in lower \mathcal{E} but break down as \mathcal{E} raises, the characteristic of the classical chaotic dynamics. For details, see Appendix A.

Lattice model. The necessary condition of the quantum chaos discussed before is the sensitivity to the initial condition. In order to confirm this sensitivity in the TL, we study a lattice model on a cubic lattice with a lattice spacing $a = 1$. For simplicity, we do not consider the environment disorder. The periodic boundary conditions are implicated while the thickness in the z -direction is finite. We label the sizes of type-I/II WSMs and the TL as $L_{I/II}$ and L , respectively. We consider minimal models describing the type-I/II WSMs on a periodic cubic lattice with Hamiltonian $H_{I/II}^l$ [47]

$$H_{I/II}^l = d_{I/II,\mu} \sigma^\mu, \quad (9)$$

where

$$\begin{aligned} d_{I/II,x} &= 2\tilde{t}(\cos k_x - \cos K_x^{I/II}) + 2\tilde{t}(1 - \cos(k_y - K_y^{I/II})) \\ &\quad + \frac{\tilde{t}}{2}(\cos 3k_x - \cos 3K_x^{I/II}) + 2\tilde{t}\gamma(1 - \cos k_z), \\ d_{I/II,y} &= 2\tilde{t}\sin(k_y - K_y^{I/II}), d_{I/II,z} = -2\tilde{t}\gamma \sin k_z, \\ d_{I,0} &= 0, d_{II,0} = -2\eta_{II}(\cos k_x - \cos K_x^{II}). \end{aligned} \quad (10)$$

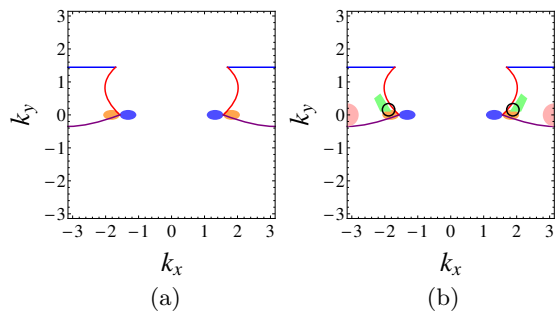


FIG. 2: (color online) The zero energy Fermi arcs and pockets in the k_x - k_y plane. (a) $\gamma_I = \gamma_{II} = \gamma_{TL} = 1$. (b) $\gamma_I = \gamma_{II} = 1$ and $\gamma_{TL} = 0.7$. The red Fermi arcs lie in the TL and connect to the Weyl nodes' images of the WSMs. The orange and blue regions correspond to the quasiparticle and quasihole Fermi pockets in the type-II WSM. The additional areas in (b) are the pink quasiparticle pockets belonging to the interval inside the horizon in the TL, and the green quasiparticle pockets are very close to the horizon from the type-II WSM side. The black circle is the area where the effective model works.

Here \tilde{t} is the hopping strength. We introduce γ , which is a z -dependent parameter (see Eq. (C2)), to fine tune the hopping strength in the z -direction. The Weyl nodes are located at $\mathbf{K}^{I/II} = (K_x^{I/II}, K_y^{I/II}, 0)$. The lattice Hamiltonian we use here is given by

$$H^l = \begin{cases} H_{II}^l, & \gamma = \gamma_{II}, n_z \leq L_{II}, \\ H_{II}^l + \xi(H_I^l - H_{II}^l), & \gamma = \gamma_{TL}, n_z \in (L_{II}, L + L_{II}], \\ H_I^l, & \gamma = \gamma_I, n_z > L + L_{II}, \end{cases} \quad (11)$$

where n_z is the lattice site index in the z -direction and $\xi = \frac{n_z - L_{II}}{L}$. In the long wave length limit, the Hamiltonian in the TL reduces to the form of Eq. (2) up to a z -dependent function which leads to a line of Weyl nodes (see Appendix C). For simplicity, we do not deal with the environment potential.

Taking $\mathbf{K}^I = (0.54\pi, 0.46\pi, 0)$, $\mathbf{K}^{II} = (0.5\pi, 0, 0)$, $\eta_{II} = 0.8\tilde{t}$ and considering a half filling lattice with $L = L_I = L_{II} = 100$, we sketch the Fermi arcs and pockets projected to the k_x - k_y plane, the colored regions in Fig. 2. There are the Fermi arcs on the surfaces of WSMs and the Fermi pockets in the type-II WSM as expected. In the TL, there are Fermi arcs that connect the type-I Weyl nodes' images and the type-II Fermi Weyl ones with the same chirality. The Weyl nodes' lines slightly deviate from these Fermi arcs and the horizon is at $\xi_h \approx 0.18$ (see Appendix C). According to the band structures of the lattice model (see Appendix B), there is no Fermi pocket in the TL for $\gamma_I = \gamma_{II} = \gamma_{TL} = 1$ (Fig. 2(a)) while Fermi pockets emerge in the TL for $\gamma_I = \gamma_{II} = 1$ and $\gamma_{TL} = 0.7$ (Fig. 2(b)).

OTOCs. The sensitivity of the initial value in quantum chaos could be measured by OTOCs [1]. We consider the simplest OTOC between the position and momentum operators in the z -direction which is measurable in the transport experiment [39]. In the semiclassical

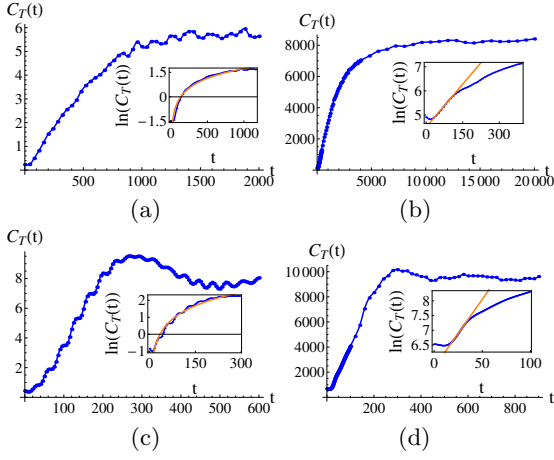


FIG. 3: (color online) The OTOCs $C_T(t)$. (a) $\gamma_{TL} = 1$ and $T = \tilde{t}/4$. The inset is a logarithmic fitting (red curve) of the $\ln C_T(t)$ in the short time. (b) $\gamma_{TL} = 1$ and $T = 2\tilde{t}/3$. The inset is a linear fitting (red line) of the $\ln C_T(t)$ in the short time. A linear region is found with $\lambda_{QL} = 0.006$. (c) $\gamma_{TL} = 0.7$ and $T = \tilde{t}/4$. The inset is a logarithmic fitting of the $\ln C_T(t)$. (d) $\gamma_{TL} = 0.7$ and $T = 2\tilde{t}/3$. The inset includes the linear region of the $\ln C_T(t)$ with $\lambda_{QL} = 0.023$.

sical limit, this OTOC describes the dependence on the initial condition of the particle motion. On the lattice, these operators, e.g., are n_z and the difference operator \hat{P}_z which acts on a state $|\psi_{\mathbf{k}}(n_z)\rangle$ where $\mathbf{k} = (k_x, k_y)$ as $\hat{P}_z|\psi_{\mathbf{k}}(n_z)\rangle = \frac{1}{2}(|\psi_{\mathbf{k}}(n_z-1)\rangle - |\psi_{\mathbf{k}}(n_z+1)\rangle)$. The OTOCs are defined by $C_T(t) = \frac{1}{Z} \text{Tr}(e^{-\beta H^I} [n_z(t), \hat{P}_z(0)]^2) = \sum_{\psi} f_{\psi} \langle \psi | [n_z(t), \hat{P}_z(0)]^2 | \psi \rangle$ where $n_z(t)$ and $\hat{P}_z(t)$ are the time-dependent operators in Heisenberg's picture. $f_{\psi} = \frac{1}{e^{\beta E_{\psi}} + 1}$ is the Fermi distribution function. More explicitly, the OTOCs are given by

$$C_T(t) = \sum_{\mathbf{k}} C_T(t, \psi_{\mathbf{k}}), \quad (12)$$

where the \mathbf{k} -dependent OTOC is given by

$$C_T(t, \psi_{\mathbf{k}}) = \sum_{\psi_1, \psi_2, \psi_3} f_{\psi} (1 - f_{\psi_1}) \times (1 - f_{\psi_2})(1 - f_{\psi_3}) \rho_{\psi_1 \psi_1} \rho_{\psi_1 \psi_2} \rho_{\psi_2 \psi_3} \rho_{\psi_3 \psi_3} \times [n_z(t)_{\psi_1 \psi_1} P_z(0)_{\psi_1 \psi_2} n_z(t)_{\psi_2 \psi_3} P_z(0)_{\psi_3 \psi_3} + \dots], \quad (13)$$

$O_{\psi \psi'} = \langle \psi | \hat{O} | \psi' \rangle$ for $\hat{O} = n_z(t)$ and $\hat{P}_z(0)$. $\rho_{\psi \psi'}$ is the probability that the state $|\psi'\rangle$ transits to the state $|\psi\rangle$ due to a disturbance. For convenience, we take $\rho_{\psi \psi'} = e^{-\beta(E_{\psi} - E_{\psi'})}$ for $E_{\psi} > E_{\psi'}$ or 1 otherwise; $O_{fi} = \langle f | \hat{O} | i \rangle$ for $\hat{O} = n_z(t)$ and $\hat{P}_z(0)$. "... " is the other three terms when explicitly writing out $[n_z(t), \hat{P}_z(0)]^2$.

In numerical calculations, we take a lower temperature $T = 1/\beta = \tilde{t}/4$ and a higher $T = 2\tilde{t}/3$. For the model with $\gamma_I = \gamma_{II} = \gamma_{TL} = 1$, the OTOC with the lower T has a small magnitude and does not have an exponential fast scrambling, as show in Fig. 3(a). In the inset in

Fig. 3(a), we see that in the very short time, the negative slope of the $\ln C_T(t)$ implies an exponential decay of the OTOC. This is because there always is a potential that binds the quasiparticles on the lattice site at the beginning. After that time period, we see a good logarithmic fitting for $\ln C_T(t)$. As the temperature raises, the fast scrambling of the OTOC appears and its magnitude becomes three order larger than that in the lower temperature as shown in Fig. 3(b). In the inset of Fig. 3(b), we see that a very short time exponential decay of the OTOC is still there. After this very short time period, we can read out a time-dependent positive quantum Lyapunov exponent $\lambda_{QL}(t)$ according to an exponential fitting $C_T(t) \sim e^{2\lambda_{QL}(t)t}$. There is a time period $t_Q \approx 100$ in which $\lambda_{QL} = 0.006$ is constant [48]. This implies the fast scrambling of the OTOC. It happens in the higher temperature is consistent with the classical chaos in the effective model because the chaos appears at higher energy. After t_Q , due to the quantum fluctuation, the fast scrambling begins to be suppressed and $\ln C_T(t)$ deviates from the linear fitting. After a long time $t_E \gtrsim 5000$, the OTOC is saturated instead of growing everlastingly in the classical chaos. This time t_E is corresponding to the Ehrenfest time. This shows a possible distinction between the quantum chaos and the classical one [40].

For $\gamma_I = \gamma_{II} = 1$ and $\gamma_{TL} = 0.7$, as shown in Fig. 3 (c) and (d), the fast scrambling in the OTOC is not seen for the lower temperature while it is there in the higher temperature, similar to that for $\gamma_{TL} = 1$. However, the time $t_Q \approx 40$ and the saturated time $t_E \approx 300$ are shorter than those for $\gamma_{TL} = 1$. This is because the green pockets emerge in Fig. 2(b), which increases the density of states and then enhances the quantum fluctuation. Meanwhile, the higher density of states also raises the quantum Lyapunov exponent in linear region about 4 times, $\lambda_{QL} = 0.023$. This means that the scrambling is much faster than that for $\gamma_{TL} = 1$.

We have yet to consider the x - y plane environment potential in the lattice model. The integrability of the model is lost if it is turned on and then the fast scrambling of the OTOC and the Ehrenfest time identify the quantum chaos.

Conclusions. We pointed out that there are emergent black/white event horizons in the TL between type-I and type-II WSMs. We found a novel surface gravity on the event horizon and the corresponding Hawking temperature may be measurable. When the Weyl nodes of type-I and type-II mismatch, the quasiparticles moving inside the horizon may be quantum chaotic. We confirm this quantum chaotic behavior in a lattice model by calculating the OTOCs of the system. Two diagnostic quantities, the quantum Lyapunov exponent and the Ehrenfest time, which characterize the quantum chaos, were determined.

This work is supported by NNSF of China with No. 11474061 (YGC, XL, YY), No. 11804223 (XL) and the ministry of science and technology of China with the grant No.2016YFA0301001 (FYL).

-
- [1] J. Maldacena, S. H. Shenker and D. Stanford, JHEP 1608, 106 (2016).
- [2] A. Kitaev, <http://online.kitp.ucsb.edu/online/joint98/kitaev/>
- [3] A. Kitaev, <http://online.kitp.ucsb.edu/online/entangled15/kitaev/> <http://online.kitp.ucsb.edu/online/entangled15/kitaev2/>
- [4] J. Maldacena and D. Stanford, Phys. Rev. D **94**, 106002 (2016).
- [5] S. Sachdev, Phys. Rev. Lett. **105**, 151602 (2010).
- [6] S. H. Shenker and D. Stanford, JHEP 1403, 067 (2014).
- [7] S. H. Shenker and D. Stanford, JHEP 1505, 132 (2015).
- [8] W. G. Unruh, Phys. Rev. Lett. **46**, 1351 (1981).
- [9] O. Lahav, A. Itah, A. Blumkin, C. Gordon, S. Rinott, A. Zayats, and J. Steinhauer, Phys. Rev. Lett. **105**, 240401 (2010).
- [10] J. Raman, M. de Nova, K. Golubkov, V. Kolobov, and J. Steinhauer, Nature **569**, 688 (2019).
- [11] A. Roldan-Molina, A. S. Nunez, and R. A. Duine, Phys. Rev. Lett. **118**, 061301 (2017).
- [12] P. Horava, Phys. Rev. Lett. **95**, 016405 (2005).
- [13] F. D. M. Haldane, Phys. Rev. Lett. **107**, 116801 (2011).
- [14] R. Z. Qiu, S. P. Kou, Z. X. Hu, X. Wan, and S. Yi, Phys. Rev. A **83**, 063633 (2011).
- [15] K. Yang, Phys. Rev. B **93**, 161302(R) (2016).
- [16] X. Luo, Y.-S. Wu, and Y. Yu, Phys. Rev. D **93**, 125005 (2016).
- [17] G. E. Volovik and M. A. Zubkov, Ann. of Phys. **356**, 255 (2015).
- [18] L. Dong and Q. Niu, Phys. Rev. B **98**, 115162 (2018).
- [19] G. E. Volovik, Pis'ma ZhETF **104**, 660 (2016).
- [20] G. E. Volovik, Physics-Uspekhi **61**, 89 (2018).
- [21] J. Nissinen and G. E. Volovik, JETP Lett. **105**, 447 (2017).
- [22] K. Zhang and G. E. Volovik, J. Low Temp. Phys. **189**, 276 (2017).
- [23] H. Q. Huang, K.-H. Jin, and F. Liu, Phys. Rev. B **98**, 121110(R) (2018).
- [24] S. W. Hawking, Nature **248**, 30 (1974); Commun. Math. Phys. **43**, 199 (1975).
- [25] J. D. Bekenstein, Phys. Rev. D **7**, 2333 (1973).
- [26] K. Hashimoto and N. Tanahashi, Phys. Rev. D **95**, 024007 (2017).
- [27] H. B. Nielsen and M. Ninomiya, Nucl. Phys. B **185**, 20 (1981). Nucl. Phys. B **193**, 173 (1981). Phys. Lett. B **130**, 389 (1983).
- [28] F.-Y. Li, X. Luo, X. Dai, Y. Yu, F. Zhang, and G. Chen, Phys. Rev. B **94**, 121105(R) (2016).
- [29] X. Wan, A. M. Turner, A. Vishwanath, and S. Y. Savrasov, Phys. Rev. B **83**, 205101 (2011).
- [30] H. M. Weng, C. Fang, Z. Fang, B. A. Bernevig, and X. Dai, Phys. Rev. X **5**, 011029 (2015).
- [31] S.-M. Huang, S.-Y. Xu, I. Belopolski, C.-C. Lee, G. Q. Chang, B. K. Wang, N. Alidoust, G. Bian, M. Neupane, C. L. Zhang, S. Jia, A. Bansil, H. Lin and M. Z. Hasan, Nat. Commun. **6**, 8373 (2015).
- [32] S. Y. Xu et al, Science **349**, 613 (2015).
- [33] B. Q. Lv et al, Phys. Rev. X **5**, 031013 (2015).
- [34] L. X. Yang et al, Nat. Phys. **11**, 728 (2015).
- [35] A. A. Soluyanov et al, Nature **527**, 495 (2015).
- [36] G. Barton, Ann. Phys. **166**, 322 (1986).
- [37] C. Yuce, A. Kilic, and A. Coruh, Phys. Scr. **74**, 114 (2006).
- [38] T. Morita, Phys. Rev. Lett. **122**, 101603 (2019).
- [39] A. I. Larkin and Y. N. Ovchinnikov, JETP **28**, 1200 (1969).
- [40] K. Hashimoto, K. Murata, R. Yoshii, JHEP **10**, 138 (2017).
- [41] S. Tchoumakov, M. Civelli, and M. O. Goerbig, Phys. Rev. B **95**, 125306 (2017).
- [42] H. Liu, J. -T. Sun, H. Q. Huang, F. Liu, and S. Meng, arXiv: 1809.00479.
- [43] G. E. Volovik, *The Universe in a Helium Droplet*, Clarendon Press, Oxford (2003).
- [44] We do not discuss the case with $|\alpha_z| > 1$. The horizon is not stable in this case.
- [45] W. H. Zurek and J. P. Paz, Phys. Rev. Lett. **72**, 2508 (1994).
- [46] P. A. Miller and S. Sarkar, Phys. Rev. E **58**, 4217 (1998).
- [47] T. M. McCormick, I. Kimchi and N. Trivedi, Phys. Rev. B **95**, 075133 (2017).
- [48] The quantum Lyapunov exponent λ_{QL} is not necessary to be exactly the same as λ_L due to the quantum correction.

Appendix A: Details on solving Eq. (6) in the main text and the classical Poincaré sections

The equations of motion (6) in the main text for the wave function $\psi = (\chi, \xi)^T$ read

$$(q_x + B_x z)\zeta - i(q_y + B_y z)\zeta + (-i\partial_z + B_z z)\chi - \alpha_x(q_x + B_x z)\chi - \alpha_z(z)(-i\partial_z + B_z z)\chi = i\partial_t \chi, \quad (\text{A1})$$

$$(q_x + B_x z)\chi + i(q_y + B_y z)\chi - (-i\partial_z + B_z z)\zeta - \alpha_x(q_x + B_x z)\zeta - \alpha_z(z)(-i\partial_z + B_z z)\zeta = i\partial_t \zeta. \quad (\text{A2})$$

Without loss of generality, we take $q_y = 0$. Notice that the $B_z z$ term is a pure gauge and can be gauged away by a gauge transformation $\psi \rightarrow \exp(-i\frac{B_z z^2}{2})\psi$. Solving

Eq. (A1), we have $\zeta = \zeta(\chi)$ and then substitute it into Eq. (A2),

$$\begin{aligned} &(((1 - \alpha_x^2)(q_x + B_x z)^2 + B_y^2 z^2) - \partial_z^2 + 2i\alpha_x(q_x + B_x z)(\alpha_z \partial_z - \partial_t) - 2\alpha_z \partial_z \partial_t + \alpha_z^2 \partial_z^2 + \partial_t^2)\chi \\ &- \frac{1}{q_x + (B_x - iB_y)z}(\alpha_x(1 + \alpha_z)B_y q_x + (\alpha_z^2 B_x - B_x + iB_y - i\alpha_z^2 B_y)\partial_z + ((1 - \alpha_z)B_x + i(1 + \alpha_z)B_y \partial_t))\chi = 0. \end{aligned} \quad (\text{A3})$$

When $q_x + B_x z \gg 1$, the second line of Eq. (A3) can be neglected. Making a transformation $\chi \rightarrow$

$\exp(i\frac{\alpha_x \alpha_z (q_x + B_x z)^2}{2B_x(1 - \alpha_z^2)})\chi$, Eq. (A3) becomes,

$$\begin{aligned} &(i\alpha_x \alpha_z (1 - \alpha_z^2)B_x + \alpha_x^2 (q_x + B_x z)^2 - (1 - \alpha_z^2)((q_x + B_x z)^2 + B_y^2 z^2))\chi \\ &+ (1 - \alpha_z^2)\partial_z^2 \chi + 2i\alpha_x (q_x + B_x z)\partial_t \chi + 2\alpha_z (1 - \alpha_z^2)\partial_t \partial_z \chi - (1 - \alpha_z^2)\partial_t^2 \chi = 0. \end{aligned} \quad (\text{A4})$$

Defining $\tilde{z} = \frac{q_x + B_x z}{B_x \sqrt{1 - \alpha_z^2}}$, Eq. (A4) reads,

$$\begin{aligned} &\partial_t^2 \chi - \partial_{\tilde{z}}^2 \chi + ((1 - \alpha_x^2 - \alpha_z^2)B_x^2 \tilde{z}^2 \\ &+ B_y^2(\sqrt{1 - \alpha_z^2} \tilde{z} - \frac{q_x}{B_x})^2)\chi - i\alpha_x \alpha_z B_x \chi \\ &- 2\alpha_z \sqrt{1 - \alpha_z^2} \partial_0 \partial_{\tilde{z}} \chi - \frac{2i\alpha_x B_x \tilde{z}}{\sqrt{1 - \alpha_z^2}} \partial_t \chi = 0. \end{aligned} \quad (\text{A5})$$

$\alpha_x^2 - \alpha_z^2)B_x^2 + (1 - \alpha_z^2)B_y^2 > 0$ or an inverted oscillator with a positive Lyapunov exponent when $\kappa < 0$. The leading order terms are the first line of Eq. (A5), and the last three terms only shift the oscillating center and the zero point energy. Since we have treated the slow-varying functions $\alpha = \alpha_{II} - \Delta\alpha_{\tilde{L}}$ as constants in the derivation of Eq. (A5), κ can be expressed as

Eq. (A5) describes a harmonic oscillator when $\kappa = (1 -$

$$\begin{aligned} \kappa(\tilde{z}) &= (\alpha_{II}^2 - 2\alpha_{II} \cdot \Delta\alpha_{\tilde{L}}^z + (\Delta\alpha_{\tilde{L}}^z)^2 - 1)B_x^2 + (\alpha_{zII}^2 - 2\alpha_{zII}\Delta\alpha_z^z + (\Delta\alpha_z^z)^2 - 1)B_y^2 \\ &= [(\alpha_{II}^2 - 1) + (\frac{2\alpha_{II} \cdot \Delta\alpha q_x}{B_x L} + \frac{\Delta\alpha^2 q_x^2}{B_x^2 L^2}) - \frac{2\sqrt{1 - \alpha_{zII}^2}(B_x \Delta\alpha \cdot \alpha_{II} L + \Delta\alpha^2 q_x)}{B_x L^2} + \frac{(\alpha_{zII}^2 - 1)\Delta\alpha^2 \tilde{z}^2}{L^2}]B_x^2 \\ &+ [(\alpha_{zII}^2 - 1) + (\frac{2\alpha_{zII}\Delta\alpha_z q_x}{B_x L} + \frac{\Delta\alpha_z^2 q_x^2}{B_x^2 L^2}) - \frac{2\sqrt{1 - \alpha_{zII}^2}(B_x \Delta\alpha_z \alpha_{zII} L + \Delta\alpha_z^2 q_x)}{B_x L^2} + \frac{(\alpha_{zII}^2 - 1)\Delta\alpha_z^2 \tilde{z}^2}{L^2}]B_y^2. \end{aligned} \quad (\text{A6})$$

Therefore the chaos related terms in Eq. (A5) reads

$$\begin{aligned} & \partial_t^2 \chi - \partial_z^2 \chi - \lambda_L^2 \tilde{z}^2 \chi - 2B_y^2 B_x^{-1} \sqrt{1 - \alpha_z^2 q_x} \tilde{z} \chi \\ & + B_y^2 B_x^{-2} q_x^2 \chi + \epsilon_3 \tilde{z}^3 \chi + \epsilon_4 \tilde{z}^4 \chi + \dots = 0, \end{aligned} \quad (\text{A7})$$

where

$$\lambda_L^2 = (\alpha_x^2,_{II} + \alpha_z^2,_{II} - 1)B_x^2 + (\alpha_z^2,_{II} - 1)B_y^2 \quad (\text{A8})$$

$$\epsilon_3 = \frac{2\sqrt{1 - \alpha_z^2,_{II}}((B_x \Delta \alpha \cdot \alpha_{II} L + \Delta \alpha^2 q_x)B_x^2 + (B_x \Delta \alpha_z \alpha_{zII} L + \Delta \alpha_z^2 q_x)B_y^2)}{B_x L^2}, \quad (\text{A9})$$

$$\epsilon_4 = \frac{(1 - \alpha_z^2,_{II})(\Delta \alpha^2 B_x^2 + \Delta \alpha_z^2 B_y^2)}{L^2}. \quad (\text{A10})$$

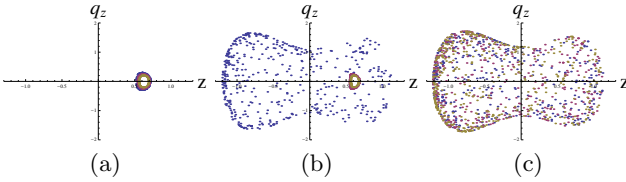


FIG. 4: The Poincaré sections for Hamiltonian (A11). For simplicity, we choose $B_x = -1$, $B_y = 1$, $\alpha_x = 2$, $\alpha_z = 0$, $\epsilon_3 = 0$, $\epsilon_4 = 4$, and $\epsilon_x = 4$. The colors (blue, purple and yellow) in the diagrams represent the Kolmogorov-Arnold-Moser(KAM) tori with different initial conditions: $q_z(0) = 0.3, 0.25$ and 0.2 , respectively, while $z(0) = 0.6$ and $x(0) = 0$. The conserved energies are: (a) $\mathcal{E} = 1$, (b) $\mathcal{E} = 1.2$, and (c) $\mathcal{E} = 1.4$. The breaking down of the KAM tori indicates the existence of classical chaos.

The first three terms in Eq. (A7) represent an inverted oscillator if $\lambda_{LII}^2 > 0$. The \tilde{z}^3 and \tilde{z}^4 terms are the quantum perturbations, and the $q_x \tilde{z}$ term is the coupling between \tilde{z} and q_x . If an environment disorder potential, say $V(x)$, is introduced, Eq. (A7) becomes not integrable and then quantum chaos appears.

To be more specific about the emergence of chaos, we consider the Poincaré sections of the classical limit of Eq. (A7) up to the \tilde{z}^4 terms. In the classical limit, $-\partial_t^2 \rightarrow E^2$ can be thought as a classical Hamiltonian, i.e.,

$$\begin{aligned} H_{classical} = & q_z^2 - \lambda_L^2 \tilde{z}^2 + \epsilon_3 \tilde{z}^3 + \epsilon_4 \tilde{z}^4 \\ & - 2B_y^2 B_x^{-1} \sqrt{1 - \alpha_z^2 q_x} \tilde{z} + B_y^2 B_x^{-2} q_x^2 + \epsilon_x x^2, \end{aligned} \quad (\text{A11})$$

where q_z is the momentum for \tilde{z} , and we take $V(x) = \epsilon_x x^2$. We draw the Poincaré sections numerically in Fig. 4 which clearly show the existence of classical chaos.

Appendix B: Band structure and Fermi energy

We give the band structures of the lattice model. Fig. 5(a) is for $\gamma_I = \gamma_{II} = \gamma_{TL} = 1$ and Fig. 5(b) is for $\gamma_I = \gamma_{II} = \gamma_{TL} = 1$. Corresponding zero energy Fermi

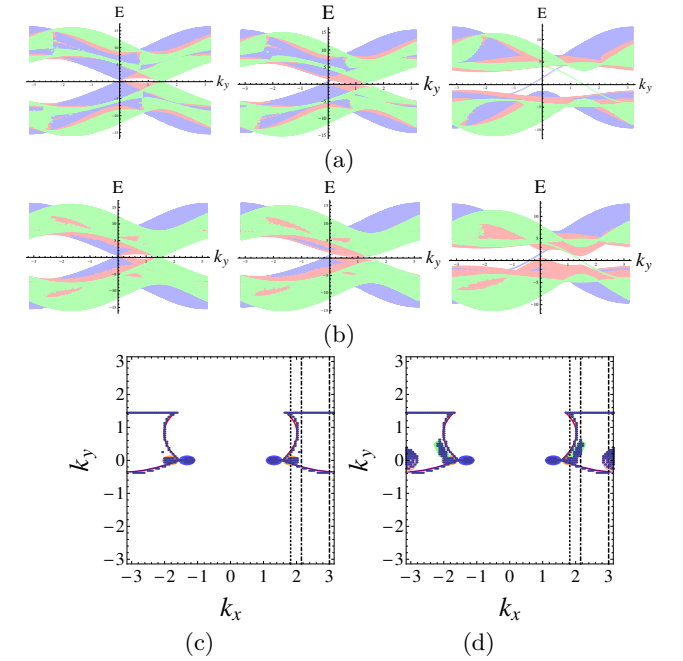


FIG. 5: The band structures of the Hamiltonian (17) in the main text with $L_I = L_{II} = L = 100$. The first panel is for $\gamma_I = \gamma_{II} = \gamma_{TL} = 1$ with $k_x = 1.8, 2.15, 3$ (see the vertical dashed lines in the third panel). The second panel is for $\gamma_I = \gamma_{II} = 1$ and $\gamma_{TL} = 0.7$ with $k_x = 1.8, 2.15, 3$. The third panel is the original data images of Fig. 2 in the main text. The zero energy state projections crossing with the vertical dashed lines can be read out from the first and second panels. The states in the red(green, blue) bands belong to the transition layer(the bulk of type-I WSM, the bulk of type-II WSM).

arcs and pockets projected to the k_x - k_y are shown in Fig. 5(c) and Fig. 5(d), respectively and they are the original data for sketching Fig. 2(a) and (b) in the main text.

Appendix C: Weyl points and horizon

Rewrite the lattice Hamiltonian (12) in the main text explicitly

$$H^l = d_\mu^l \sigma^\mu, \quad (\text{C1})$$

where

$$d_\mu^l = \begin{cases} d_{\mu,II}^l, & \gamma = \gamma_{II}, \text{ for } n_z < n_{II}, \\ d_{\mu,II}^l + \xi(d_{\mu,I}^l - d_{\mu,II}^l), & \gamma = \gamma_{TL}, \text{ for } n_{II} < n_z < n_I, \\ d_{\mu,I}^l, & \gamma = \gamma_I, \text{ for } n_z > n_I, \end{cases} \quad (\text{C2})$$

and

$$\begin{aligned} d_{I/II,x} &= 2\tilde{t}(\cos k_x - \cos K_x^{I/II}) + 2\tilde{t}(1 - \cos(k_y - K_y^{I/II})) \\ &\quad + \frac{\tilde{t}}{2}(\cos 3k_x - \cos 3K_x^{I/II}) + 2\tilde{t}\gamma(1 - \cos k_z), \\ d_{I/II,y} &= 2\tilde{t}\sin(k_y - K_y^{I/II}), \quad d_{I/II,z} = -2\tilde{t}\gamma \sin k_z, \\ d_{I,0} &= 0, \quad d_{II,0} = -2\eta_{II}(\cos k_x - \cos K_x^{II}), \end{aligned} \quad (\text{C3})$$

where n_z is the lattice site index in the z -direction and $\xi = \frac{n_z - L_{II}}{L}$. Then the Weyl points are determined by

$$d_i^l = 0, \quad i = x, y, z. \quad (\text{C4})$$

At Weyl points,

$$\partial_i d_j^l = 0, \quad \text{if } i \neq j. \quad (\text{C5})$$

The Weyl points in the transition layer are running as ξ and their projection to the k_x - k_y plane is depicted in Fig. 6(a). Notice that these Weyl points do not lie on the Fermi surface because of the interlayer coupling. If the transition layer is replaced by an insulating layer with a large band gap, then there will be ordinary Fermi arcs that connect Weyl nodes with opposite chiralities in the type-I(II) WSM on the top(bottom) surface of the insulating layer. After turning on the hopping term between the type-I and type-II WSMs in the transition layer, the Fermi arcs will reconstruct. Changing from the surface Fermi arcs into the ones connecting type-I and type-II

Weyl nodes with the same chirality inside the transition layer (see the red Fermi arcs in Fig. 6(a)).

Expanding the Hamiltonian (C2) around the Weyl points and comparing the result with the effective Hamiltonians (3) and (4) in the main text, one obtains,

$$|\alpha| = \sqrt{\sum_{i=x,y,z} (\partial_i d_0^l / \partial_i d_i^l)^2} = |\partial_x d_0^l / \partial_x d_x^l|. \quad (\text{C6})$$

The horizon can be obtained by solving $|\alpha| = 1$ which is at $\xi_h \approx 0.18$, reading out from Fig. 6(b).

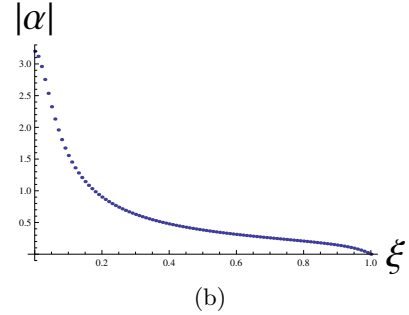
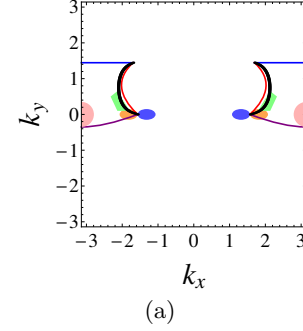


FIG. 6: (color online) (a) The Weyl points in the transition layer (black curves). We copy the zero energy regions in Fig. 2(b) of the main text for the reference. (b) The function $|\alpha|$ of ξ . $|\alpha(\xi_h)| = 1$ determines the horizon.